Available online at www.sciencedirect.com

SciVerse ScienceDirect

Ceramics International 39 (2013) 6887–6897

CERAMICS INTERNATIONAL

www.elsevier.com/locate/ceramint

Feedstock properties and injection molding simulations of bimodal mixtures of nanoscale and microscale aluminum nitride

Kunal H. Kate[a], Ravi K. Enneti[b], Valmikanathan P. Onbattuvelli[c], Sundar V. Atre[a,*]

[a]*Oregon State University, Corvallis, OR, USA*
[b]*Global Tungsten Powders, Towanda, PA, USA*
[c]*Intel Corporation, Chandler, AZ, USA*

Received 5 December 2012; received in revised form 25 January 2013; accepted 11 February 2013
Available online 18 February 2013

Abstract

Powder injection molding (PIM) is useful to manufacture small, complex metal and ceramic components in high production volumes. Mixing nanoparticles (n) with microparticles (μ) has been previously identified in our research group as a promising approach to achieve high sintered density and low shrinkage in injection molded AlN. Sintering studies showed a liquid phase formation at ~1500 °C in bimodal μ–n AlN samples, a temperature that is atleast 100 °C lower than typically reported values in the literature. Sintered parts of bimodal μ–n AlN mixtures exhibited comparable sintered density but lower shrinkage (~14%) than corresponding monomodal μ-AlN (~20%). These benefits in sintered attributes are a direct consequence of a significant increase in the packing density in powder–polymer mixtures with the addition of nanoparticles. However, there are few studies focused on understanding the effects of nanoparticle addition on the rheological and thermal properties of the bimodal feedstock. The present study combines experimental measurement feedstock properties with models for estimating properties over a range of powder content. The properties were subsequently used in mold-filling simulations to understand the effects of powder content on process parameters and defect evolution in PIM. These protocols and findings can be used to improve PIM design practices in material selection, component geometry attributes, and optimized process parameters.

Keywords: Powder injection molding; Nanoparticles; Microparticles; Feedstock properties; Simulations

1. Introduction

Powder injection molding (PIM) has emerged as the primary technology to economically manufacture small, complex metal and ceramic components in high production volumes [1]. The PIM process utilizes a mixture of metal or ceramic powder and polymer (feedstock) to shape the component. In subsequent processing steps, the polymer is removed from the shaped component and the part is sintered at high temperature to achieve the required density and functional properties [2].

Feedstock composition and properties play a critical role in the success of PIM. A failure to optimize feedstock compositions could result in the formation of defects such as weldlines, cracks and warpage during the injection molding process. Most defects formed during injection molding get enlarged during subsequent sintering operations, resulting in the production of low-quality parts after undergoing significant value-addition steps [3]. Thus, understanding the effects of powder characteristics on feedstock properties is critical to the success of PIM. In order to eliminate molding defects, one common practice in PIM is to lower the powder–polymer ratio in the feedstock, thereby enhancing the flowability and green strength of the part during injection molding. However lowering the powder content in the feedstock will also result in a higher shrinkage following sintering, resulting in poor dimensional control of the final parts.

---

*Corresponding author.
E-mail addresses: ravienneti@gmail.com (R.K. Enneti), sundar.atre@oregonstate.edu (S.V. Atre).

0272-8842/$ - see front matter
http://dx.doi.org/10.1016/j.ceramint.2013.02.023

The relation between final dimensions of the sintered part and the initial volume fraction of powder, ϕ_p, is given by [4]

$$Y = 1 - \left(\frac{\phi_p}{f_s}\right)^{1/3} \qquad (1)$$

where Y is the linear shrinkage factor and f_s is the fractional sintered density. This inter-relationship between part shrinkage, sintered density and initial volume fraction of powder is shown in Fig. 1. It can be seen that for a given sintered density, parts with lower volume fraction of powder in the feedstock undergo larger shrinkage. Sintering at a lower temperature in order to minimize shrinkage is not a viable solution since it will result in lower density and inferior properties of the component.

The use of bimodal mixtures of nanoscale and microscale particles has been recently identified as a promising approach to fabricate parts with high sintered density and low shrinkage in recent studies emerging from our research group [5–7]. The sintering studies showed the formation of liquid phase at 1500 °C in bimodal μ–n AlN samples, a temperature that is ~100 °C lower than typically reported values in the literature. The sintered parts of bimodal μ–n AlN mixtures exhibited comparable sintered density but lower shrinkage (~14%) than the corresponding monomodal mixtures (~20%) [5–7]. Our prior research study [8] also showed significant increase in the maximum powder content in powder–polymer mixture with the addition of nanoparticles. For example, a maximum powder content of 90 wt% (71 vol%) was achieved in bimodal μ–n AlN powder–polymer mixtures. In contrast, monomodal μ-AlN powder–polymer mixtures had a maximum powder content of only 81 wt% (54 vol%) [8]. However, an understanding of the effect of nanoparticles on PIM feedstock properties has not been reported in the literature. This gap in prior reports is significant, since nanoparticles typically exhibit poor packing behavior and show a high tendency for agglomeration, negatively impacting the rheological behavior and homogeneity of the feedstock [8]. The current study is focused on understanding the effect of powder content on the rheological, mechanical and thermal properties of bimodal μ–n AlN feedstocks.

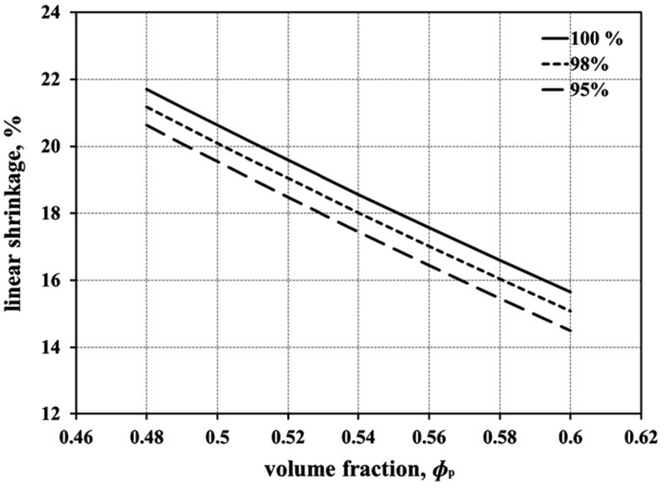

Fig. 1. Dependence of linear shrinkage on final sintered density and different volume fractions of powder, ϕ_p, using Eq. (1).

In PIM design, it is important to know the injection molding behavior at different powder–polymer compositions so as to understand the trade-offs between ease-of-fabrication, process throughput, and part quality at the design stage. Injection molding design simulations rely on a numerous feedstock properties as input data [9]. In order to maximize the benefit of these design tools, there is a critical need to determine the influence of material composition on thermal, rheological and mechanical properties of powder–polymer mixtures. A limited database of materials properties at different powder–polymer compositions is a significant challenge that needs to be addressed in order to conduct accurate computer simulations that aid part and mold design in PIM. However, accurate material property measurements can be expensive and time-consuming. In order to resolve these conflicting challenges it is hypothesized that experimental measurements of material properties of a filled polymer at a specific filler content combined with similar measurements of unfilled polymer will be adequate to estimate the dependence of properties on filler content using mathematical models.

In the present study, the changes in feedstock properties as a result of varying volume fraction of powder were estimated using experimental measurements and semi-empirical models. Subsequently, the effects of feedstock properties on mold-filling behavior and defect formation were studied using the Autodesk Moldflow Insight simulation platform. The results from the present study will provide a quantitative understanding of the influence of material composition on feedstock properties and mold-filling behavior; resulting in the development of new material compositions that will aid in the designing and manufacturing of complex sintered components with high density and low shrinkage. The simulation results will also assist in selecting component geometrical attributes and optimizing process parameters while eliminating expensive and time-consuming trial-and-error practices prevalent in PIM.

2. Experimental materials and methods

Commercially available AlN (median particle size: d_{50}~1 μm and d_{50}~20 nm) and Y_2O_3 (d_{50}~50 nm) were used as the starting materials in as received condition. The bimodal μ–n AlN mixtures contained 82 wt% larger (μ) and 18 wt% finer (n) AlN powders. 5 wt% Y_2O_3 was added to the powder mixture on the basis of AlN. The vol% of the powders was 60%. The SEM micrograph of the powder is shown in Fig. 2. A multi-component binder system comprising of paraffin wax (PW), polypropylene (PP), polyethylene-*g*-maleic anhydride (LDPE-*g*-MA) and stearic acid (SA) was used in the current study. Details of the composition and mixing preparations are provided elsewhere [10].

The rheological characteristics of the unfilled binder and bimodal μ–n AlN feedstock were examined on a Gottfert Rheograph 2003 capillary rheometer at different shear rates and temperatures. The testing was carried out in accordance with ASTM D3835. The temperature range was selected between the highest melting temperature and the lowest degradation temperature of the binder system. The barrel of inner diameter 1 mm and die length 20 mm was used. Torque rheometry was performed in the Intelli-Torque Plasticorder (Brabender) in order to determine the maximum packing density of the powder–polymer mixture. Twin-screw extrusion of AlN feedstocks was performed with an Entek co-rotating 27 mm twin screw extruder with an L/D ratio of 40 and pelletized for further use. Injection molding was performed on an Arburg 221M injection–molding machine. Thermogravimetric analysis (TGA) was performed on the binder mixture as well as the bimodal μ–n AlN feedstock in order to confirm the powder weight fraction in the feedstock. TGA measurements were performed on a TA-Q500 (TA instruments) thermal system operated under nitrogen flow in the temperature range of 50–600 °C with a heating rate of 20 °C/min.

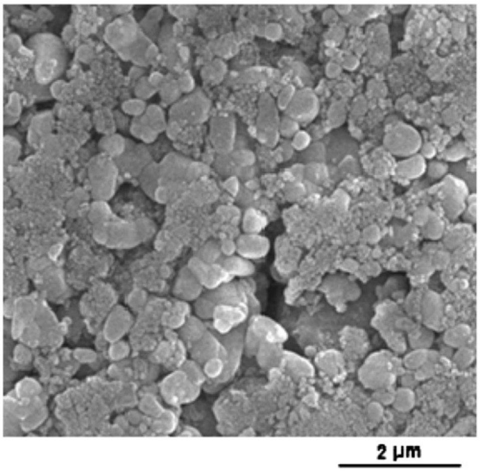

Fig. 2. SEM of the bimodal μ–n AlN powder mixture used in the present study.

A K-System II thermal conductivity system was used to evaluate the thermal conductivity of the binder mixture

Table 1
Models used in the present study to estimate the feedstock properties.

Property	Empirical relation (Eq. no)	
Viscosity	$\eta_c = \frac{\eta_b}{[1-(\phi_p/\phi_{max})]^2}$	(2)
	$\eta = \frac{\eta_0}{1+(\eta_0\gamma/\tau^*)^{1-n}}$	(3)
	$\eta_0 = D_1 \exp\left[-\frac{A_1(T-T^*)}{A_2+(T-T^*)}\right]$	(4)
Specific volume	$\upsilon_c = X_p\upsilon_p + \upsilon_b(1-X_f)$	(5)
	$\upsilon(T,p) = \upsilon_o(T)\left[1-C\ln\left(1+\frac{p}{B(T)}\right)+\upsilon_t(T,p)\right]$	(6)
	$T > T_t: \quad \upsilon_o = b_{1m}+b_{2m}(T-b_5)B(T) = b_{3m}e^{[-b_{4m}(T-b_5)]}\upsilon_t(T,p) = 0$	(7)
	$T < T_t: \quad \upsilon_o = b_{1s}+b_{2s}(T-b_5)B(T) = b_{2s}e^{[-b_{4s}(T-b_5]}\upsilon_t(T,p) = b_7e^{[b_8(T-b_5)-(b_9p)]}$	(8)
Density	$\frac{1}{\rho_c} = \frac{X_b}{\rho_b}+\frac{X_p}{\rho_p}$	(9)
Mass fraction	$X_p = \frac{\phi_p\rho_p}{\phi_p\rho_p+\phi_b\rho_b}$	(10)
	$X_b = \frac{\phi_b\rho_b}{\phi_p\rho_p+\phi_b\rho_b}$	(11)
Specific heat	$C_{pc} = [C_{p_b}X_b + C_{p_p}X_p][1+AX_bX_p]$	(12)
Thermal conductivity	$\lambda_c = \lambda_b\phi_b+\lambda_p\phi_p$	(13)
Coefficient of thermal expansion	$\alpha_c = X_p\alpha_p+\alpha_b(1-X_p)$	(14)
Elastic and shear modulus	$E_c = E_pX_p+E_b(1-X_b)$	(15)

and the bimodal μ–n AlN feedstock. The testing was carried out in accordance with ASTM D5930. The initial temperature was 190 °C and final temperature was 30 °C. The probe voltage was kept at 4 V and acquisition time of 45 s. Specific heat measurements were carried out on Perkin Elmer DSC7 equipment in accordance with ASTM E1269. The testing was done with an initial temperature of 190 °C and final temperature of 20 °C. The cooling rate was kept constant of 20 °C/min. A Gnomix PVT apparatus was used to find the pressure–volume–temperature (PVT) relationships of the binder and bimodal μ–n AlN feedstock materials. The tests were performed in accordance with ASTM D792. The pellets were dried for 4 h at 70 °C under vacuum. The measurement type used was isothermal heating scan with a heating rate of approximately 3 °C/min.

Two heat sink designs were investigated in this study using the Autodesk Solidworks 2011 software. The Autodesk Moldflow Insight 2011 software was used for simulating the injection conditions of two heat-sink components. The part was meshed using an automated solid 3D meshing protocol based on finite element analysis. The process settings were 303 K for the mold temperature and 433 K for the melt temperature. Simulations were conducted for a fill-and-pack type condition in order to understand the molding–filling behavior as well as packing characteristics as a function of material composition.

3. Results and discussion

3.1. Properties

The experimentally determined physical properties of bimodal μ–n AlN powder-polymer mixtures at 0 and 0.6 volume fractions were used to estimate properties of bimodal μ–n AlN powder–polymer mixtures with 0.52–0.58 volume fractions. Several mathematical models have been published in the literature to predict various feedstock properties that are necessary as input data for conducting mold-filling simulations [11–28]. The models used in the present study were selected after carrying out an in-depth statistical analysis of various published models fitted to literature data on experimentally measured powder–polymer mixture properties [29]. The models used to estimate various properties of bimodal μ–n AlN are summarized in Table 1. The descriptions of symbols in the equations are detailed in Table 2. Additionally, the viscosity and PVT data required curve fitting to extract constants required as input for mold filling simulations using the Autodesk Moldflow Insight software.

A simplified Krieger–Dougherty [7] viscosity model was used as it is suitable for predicting viscosity values at higher volume fractions of powder (Eq. (2)). The Cross-WLF model [11] was used to model the viscosity

Table 2
Descriptions of the symbols used in empirical relations presented in Table 1.

Symbol	Description	Symbol	Description
η_b	Viscosity of binder	ρ_p	Density of powder
η_c	Viscosity of composite	X_c	Mass fraction of composite
$\boldsymbol{\phi}_p$	Volume fraction of powder	X_b	Mass fraction of binder
ϕ_{max}	Maximum volume fraction	X_p	Mass fraction of powder
η	Melt viscosity	C_p	Specific heat
η_0	Zero shear viscosity	λ	Thermal conductivity
γ	Shear rate	α	Thermal expansion coefficient
τ^*	Critical stress level at the transition to shear thinning	E	Elastic or shear modulus
n	Power law index in the high shear rate regime	υ	Specific volume
T	Temperature	$\upsilon\ (T,p)$	Specific volume at a given temperature and pressure
T^*, D_1 and A_1	Curve-fitted coefficients	υ_o	Specific volume at zero gauge pressure
T_t	Volumetric transition temperature	p	Pressure
A_2	WLF constant, 51.6 K	C	Constant, 0.0894
ρ_c	Density of composite	b_{1s}, b_{2s}, b_{3s}, b_{4s},b_5, b_7,b_8,b_9	Curve-fitted coefficients
ρ_b	Density of binder	b_{1m}, b_{2m}, b_{3m}, b_{4m}, b_5, b_6	Curve-fitted coefficients

Table 3
Cross–WLF constants for feedstocks with different volume fractions of bimodal μ–n AlN powders. The highlighted data (0 and 0.6 volume fraction) in the table are obtained from experiments.

Cross-WLF constants	Volume fraction, ϕ_p					
	0	0.52	0.54	0.56	0.58	**0.6**
n^*	**0.40**	0.24	0.21	0.18	0.13	**0.05**
τ, Pa	**793**	30,070	44,000	68,000	117,000	**162,000**
D_1, Pa s	$\mathbf{4.29 \times 10^{23}}$	1.08×10^{14}	1.83×10^{14}	4.29×10^{14}	1.71×10^{15}	$\mathbf{9.13 \times 10^{19}}$
T, K	**333.00**	265	266	265	265	**263**
A_1	**78.13**	29.55	29.56	29.55	29.55	**29.54**
A_2, K	**51.60**	51.60	51.60	51.60	51.60	**51.60**

dependence of any given powder–polymer mixture on shear rate (Eq. (3)). The temperature dependence of viscosity of any powder–polymer mixture [11] was estimated using Eq. (4). The values of the coefficients (T^*, D_1 and A_1) were obtained by curve-fitting the estimated viscosity for different volume fractions of powder at various shear rates and temperatures and are summarized in Table 3. Fig. 3 shows the shear-rate dependence of viscosity for bimodal μ–n AlN at 413 and 433 K. The zero-shear viscosity was estimated from the plateau region at low shear rate while the power law index was obtained from the slope at higher shear rates. It can be observed that the zero-shear viscosity increased considerably with small increases in volume fraction, ϕ_p, in the range of interest. The curve-fitted WLF parameters n, τ^*, D_1, T^*, A_1 and A_2 were estimated for temperatures between 413 K and 433 K. The values estimated for n and τ^* for each temperature were then averaged for individual volume fractions of powder. The values of remaining parameters did not vary appreciably with an increase in temperature within the experimental range. The power law index, n, decreased from 0.24 to 0.05 with an increase in volume fraction from 0.52 to 0.60. Similarly, τ^* increased from 3×10^4 to 1.6×10^5 Pa with an increase in volume fraction from 0.52 to 0.60. There was no change in transition temperature (T^*) at which the material exhibits a change from Newtonian to shear-thinning behavior on increasing shear rates with increase in volume fraction of the powder.

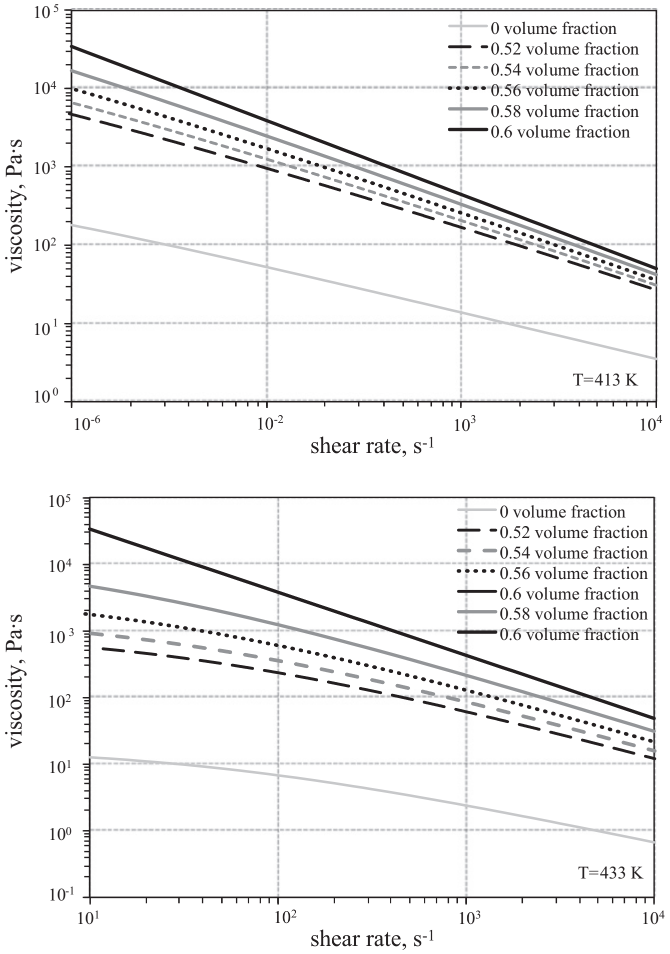

Fig. 3. Comparison of viscosity with shear rate at 413 K (top) and 433 K (bottom) for different volume fractions of bimodal μ–n AlN powder.

The specific volume was calculated using the general rule-of-mixtures as shown in Eq. (5) [12]. The injection molding software platform uses a two-domain Tait [13] equation (Eq. (6)) for generating viscosity values at different volume fractions of powder. The parameter, B, accounts for the pressure sensitivity of the material and is separately defined for the solid and melt regions. For the upper bound, when $T > T_t$ (volumetric transition temperature), B is given by Eq. (7). For the lower bound, when $T < T_t$, the parameter, B, is given by Eq. (8).

The dependence of the volumetric transition temperature, T_t on pressure can be given by $T_t(p) = b_5 + b_6(p)$,

Table 4
Dual-domain Tait constants for feedstocks with different volume fractions of bimodal μ–n AlN powders. The highlighted data (0 and 0.6 volume fraction) in the table are obtained from experiments.

Dual-domain Tait constants	**Volume fraction, ϕ_p**						
	0	0.5	0.52	0.54	0.56	0.58	**0.6**
b_5, K	**336**	336	336	336	336	336	**336**
b_6, K/Pa	$\mathbf{1.5 \times 10^{-7}}$	1.6×10^{-7}	1.6×10^{-7}	1.6×10^{-7}	1.6×10^{-7}	1.6×10^{-7}	$\mathbf{1.6 \times 10^{-7}}$
b_{1m}, m^3/kg	$\mathbf{1.3 \times 10^{-3}}$	5.1×10^{-4}	4.9×10^{-4}	4.8×10^{-4}	4.7×10^{-4}	4.6×10^{-4}	$\mathbf{4.5 \times 10^{-4}}$
b_{2m} m^3/kg K	$\mathbf{1.3 \times 10^{-6}}$	2.8×10^{-7}	2.6×10^{-7}	2.4×10^{-7}	2.2×10^{-7}	2.0×10^{-7}	$\mathbf{1.8 \times 10^{-7}}$
b_{3m}, Pa	$\mathbf{1.3 \times 10^{8}}$	3.4×10^{8}	3.4×10^{8}	3.4×10^{8}	3.4×10^{8}	3.4×10^{8}	$\mathbf{3.4 \times 10^{8}}$
b_{4m}, K^{-1}	$\mathbf{6.0 \times 10^{-3}}$	4.0×10^{-3}	4.0×10^{-3}	4.0×10^{-3}	4.0×10^{-3}	4.0×10^{-3}	$\mathbf{4.0 \times 10^{-3}}$
b_{1s}, m^3/kg	$\mathbf{1.2 \times 10^{-3}}$	4.9×10^{-4}	4.8×10^{-4}	4.7×10^{-4}	4.6×10^{-4}	4.5×10^{-4}	$\mathbf{4.3 \times 10^{-4}}$
b_{2s}, m^3/kg K	$\mathbf{8.6 \times 10^{-7}}$	2.6×10^{-7}	2.3×10^{-7}	2.0×10^{-7}	1.8×10^{-7}	1.5×10^{-7}	$\mathbf{1.5 \times 10^{-7}}$
b_{3s}, Pa	$\mathbf{2.4 \times 10^{8}}$	5.0×10^{8}	5.0×10^{8}	5.0×10^{8}	5.0×10^{8}	5.0×10^{8}	$\mathbf{5.0 \times 10^{8}}$
b_{4s}, K^{-1}	$\mathbf{4.2 \times 10^{-3}}$	6.5×10^{-3}	4.3×10^{-3}	9.7×10^{-3}	9.2×10^{-2}	1.1×10^{-2}	$\mathbf{1.0 \times 10^{-2}}$
b_7, m^3/kg	$\mathbf{8.5 \times 10^{-5}}$	2.0×10^{-6}	3.8×10^{-6}	2.8×10^{-6}	2.9×10^{-6}	8.7×10^{-7}	$\mathbf{8.9 \times 10^{-6}}$
b_8, K^{-1}	$\mathbf{6.7 \times 10^{-2}}$	2.5×10^{-2}	1.2×10^{-2}	3.9×10^{-2}	4.0×10^{-2}	6.1×10^{-2}	$\mathbf{1.3 \times 10^{-1}}$
b_9, Pa^{-1}	$\mathbf{1.4 \times 10^{-8}}$	2.2×10^{-8}	2.2×10^{-8}	2.2×10^{-8}	2.2×10^{-8}	2.2×10^{-8}	$\mathbf{2.2 \times 10^{-8}}$

where b_5 and b_6 are the curve-fitted coefficients. The values of these coefficients are summarized in Table 4. Fig. 4 shows the plots of specific volumes at 0, 100, and 200 MPa. The specific volume decreases with an increase in volume fraction of bimodal μ–n AlN. The dual-domain Tait constants were estimated using curve fitting for 0, 50, 100, 150, 200 MPa for volume fractions of 0, 0.52 to 0.60 bimodal μ–n AlN. The parameters, b_5, b_6, b_9, b_{3m}, b_{4m}, b_{3s} and b_{4s} did not vary in the range of 0.52–0.60 volume fraction of bimodal μ–n AlN. The parameters b_{1m}, b_{2m}, b_{1s} and b_{2s} showed a minor decrease on increasing the volume fractions from 0.52 to 0.60. Parameters, b_7 and b_8 increased with the increase in volume fraction of powder.

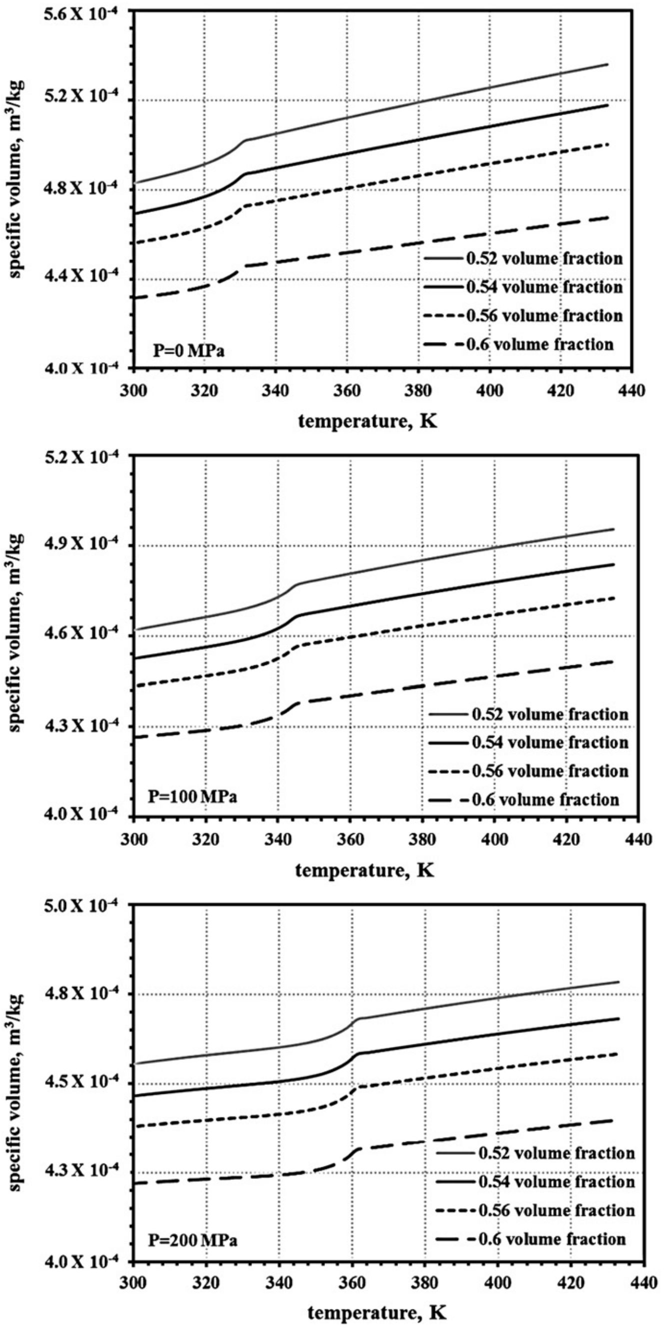

Fig. 4. PVT behavior for different volume fractions of bimodal μ–n AlN powder at 0, 100, and 200 MPa.

An inverse rule-of-mixture [12] was used to estimate the melt and solid density, as shown in Eq. (9). Furthermore, the mass fractions for powder and binder were calculated using Eqs. (10) and (11). The variation of melt and solid density as a function of volume fraction of bimodal μ–n AlN is shown in Table 5. The melt and solid density values increased with an increase in powder volume fraction. The melt density increased from 1950 to 2160 kg/m^3 and solid density increased from 2120 to 2310 kg/m^3 with an increase in volume fraction of bimodal μ–n AlN from 0.52 to 0.60. The data in Table 5 indicates a $\pm 4\%$ variation in melt and solid density as a result of a $\pm 7\%$ change in the volume fraction of bimodal μ–n AlN.

The specific heat of powder–polymer mixtures has been estimated by different mixing rules [14–18]. In this study, a model that has been successfully applied to mixtures with high volume fraction fillers [15] was used as shown in Eq. (12). The parameter, A, is a correction factor assumed to be 0.2 for spherical particles. The specific heat values calculated for different volume fractions of powder at various temperatures are shown in Table 6. The specific heat of the feedstock decreased with the increase in volume fraction of powders. As a specific example, a change of volume fraction from 0.52 to 0.60 at 443 K resulted in a decrease in specific

Table 5
Comparison of melt and solid densities for feedstocks with different volume fractions of bimodal μ–n AlN powders. The highlighted data (0 and 0.6 volume fraction) in the table are obtained from experiments.

Volume fraction of powder, ϕ_p	**Melt density, kg/m^3**	**Solid density, kg/m^3**
0	**730**	**880**
0.52	1950	2120
0.54	2000	2170
0.56	2050	2210
0.58	2110	2260
0.6	**2160**	**2310**

Table 6
Specific heat capacity values at various temperatures for feedstocks with different volume fractions of bimodal μ–n AlN powders. The highlighted data (0 and 0.6 volume fraction) in the table are obtained from experiments.

Volume fraction of powder, ϕ_p	**Temperature, K**						
	273	293	303	322	331	384	443
	Specific heat capacity, C_p, J/kg K						
0	**2077**	**3360**	**3840**	**4894**	**3484**	**3484**	**2528**
0.52	1006	1290	1610	3050	1480	1360	1490
0.54	1004	1260	1570	3010	1420	1350	1470
0.56	1002	1000	1540	2980	1370	1335	1450
0.58	1000	1210	1505	2950	1320	1320	1430
0.6	**998**	**1186**	**1472**	**2915**	**1274**	**1315**	**1413**

Table 7
Thermal conductivity for feedstocks with different volume fractions of bimodal μ–n AlN powder. The highlighted data (0 and 0.6 volume fraction) in the table are obtained from experiments.

Volume fraction of powder, ϕ_p	Temperature, K						
	315	336	356	377	397	417	436
	Thermal conductivity, W/m K						
0	**0.2**	**0.2**	**0.2**	**0.2**	**0.2**	**0.2**	**0.2**
0.52	2.7	2.7	2.9	2.0	2.1	3.0	1.9
0.54	2.8	2.8	2.9	2.1	2.2	3.1	2.0
0.56	2.9	2.9	3.1	2.1	2.2	3.2	2.0
0.58	3.0	3.0	3.2	2.2	2.3	3.3	2.1
0.6	**3.1**	**3.1**	**3.3**	**2.3**	**2.4**	**3.4**	**2.2**

Table 8
Coefficient of thermal expansion for feedstocks with different volume fractions of bimodal μ–n AlN powder. The highlighted data (0 and 0.6 volume fraction) in the table are obtained from experiments.

Volume fraction of powder, ϕ_p	CTE, 10^{-5} K^{-1}
0	**5.65**
0.52	1.94
0.54	1.9
0.56	1.8
0.58	1.77
0.60	**1.72**

Table 9
Elastic and shear modulus values for feedstocks with different volume fractions of bimodal μ–n AlN powder. The highlighted data (0 and 0.6 volume fraction) in the table are obtained from experiments.

Volume fraction of powder, ϕ_p	Elastic modulus, MPa	Shear modulus, MPa
0	**2560**	**930**
0.52	18,900	7120
0.54	19,490	7360
0.56	20,110	7600
0.58	20,740	7840
0.6	**21,370**	**8075**

heat from 1490 to 1413 J/g K. The data in Table 6 indicates a ±2% change in specific heat results from a ±7% change in the volume fraction of bimodal μ–n AlN.

Several equations have been used to predict thermal conductivity of a composite at different filler concentrations [14,16–25]. In this study, a general rule-of-mixtures model [12] was used as represented in Eq. (13). The estimated values of thermal conductivity as a function of volume fraction of powder at various temperatures are shown in Table 7. It can be seen that the thermal conductivity increases with the increase in volume fraction of bimodal μ–n AlN. For example, the thermal conductivity increased from 1.9 to 2.2 W/m K with an increase in volume fraction from 0.52 to 0.6 bimodal μ–n AlN at 436 K. The data presented in Table 7 indicate that a ±8% variation in thermal conductivity results from a ±7% change in volume fraction of bimodal μ–n AlN. The data in Tables 6 and 7 also shows absence of uniform decrease in specific heat and thermal conductivity of feedstock with increase in the temperature. The change in crystalline and amorphous phases of the binder in the feedstock with increase in temperature is understood to be the reason behind the observed trend [1].

The coefficient of thermal expansion (CTE) of powder–polymer mixtures can be calculated using several models [18,25–28]. In this paper, a first order model was used [18] as shown in Eq. (14). The CTE data are as shown in Table 8. The data in Table 8 clearly shows a decrease in CTE with an increase in volume fraction of bimodal μ–n AlN. Typically in the range of 0.52–0.60 volume fractions, the CTE varied between 1.9E−5 and 1.7E−5 K^{-1} which represents a ±12.8% variation in CTE for a ±7% change in volume fraction of bimodal μ–n AlN in the powder–polymer mixtures.

The Voigt model [18] was used to predict the elastic and shear modulus as shown in Eq. (15). The elastic and shear modulus values were estimated at different volume fractions of powder and are shown in Table 9. The elastic and shear modulus values were found to increase with an increase in volume fraction of bimodal μ–n AlN. Typically, in the range of 0.52–0.60 volume fraction, the elastic modulus increased between $\sim 1.9\times10^4$ and $\sim 2.1\times10^4$ MPa and shear modulus varies between 7.1×10^3 and

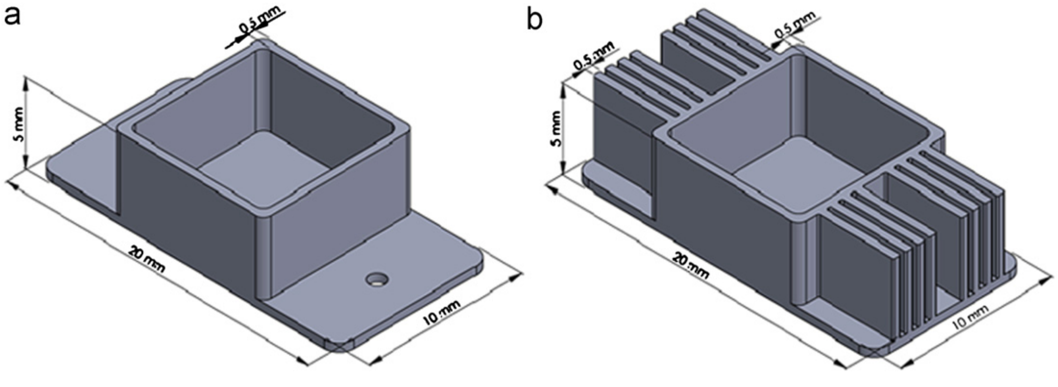

Fig. 5. Mold geometry used in injection molding simulations: (a) simple heat-sink substrate without fins and (b) heat sink substrate with fins.

8.1×10^3 MPa which represents a ± 6.3% variation in the elastic and shear modulus for a ± 7% change in volume fraction of bimodal μ–n AlN in the powder–polymer mixtures.

3.2. Simulation results

Simulations were conducted for 0.52–0.60 volume fraction of bimodal μ–n AlN at 433 K melt temperature and 303 K

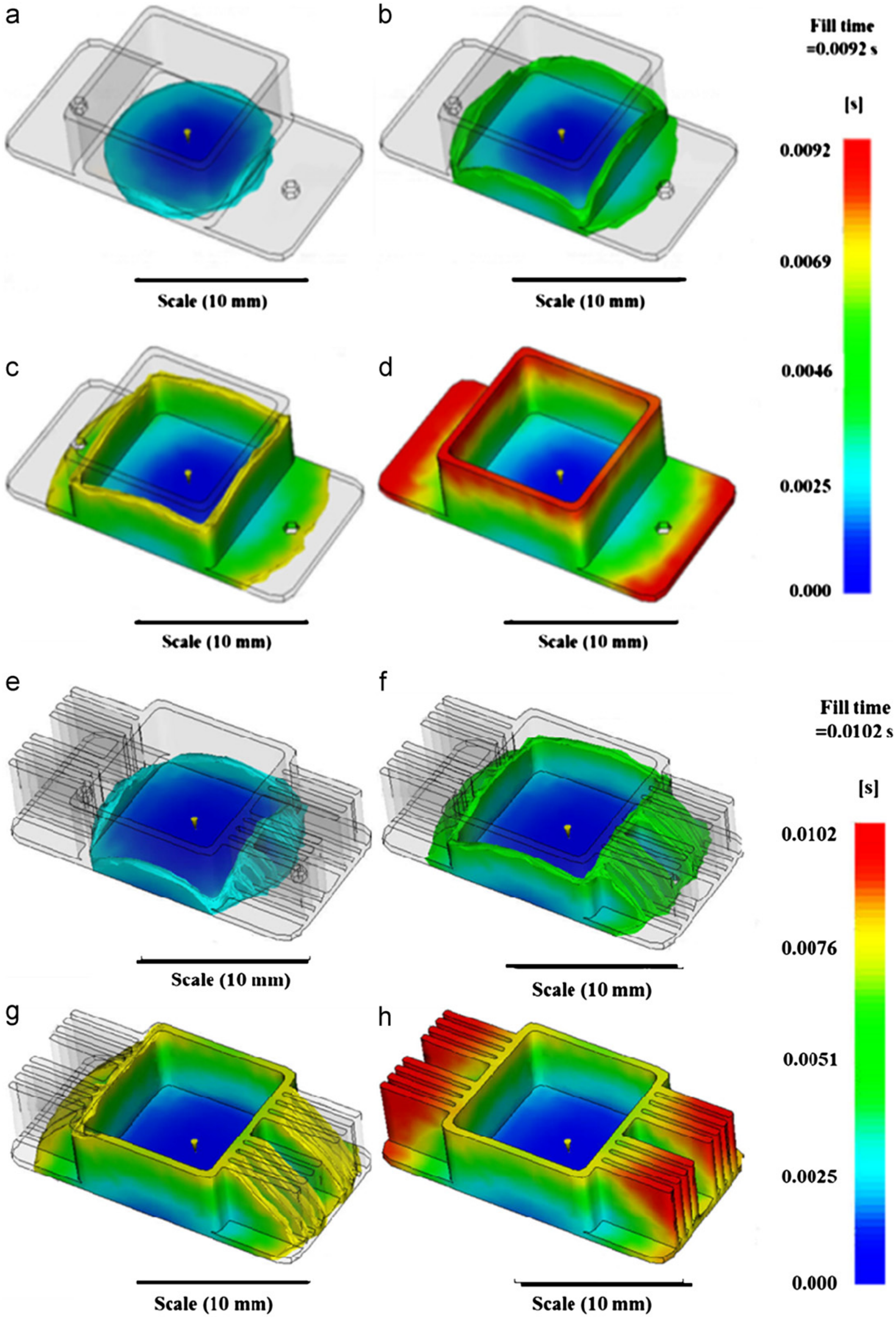

Fig. 6. (a–d) Progressive filling of the heat sink substrate without fins shown in Fig. 5(a) for the 0.60 volume fraction bimodal μ–n AlN feedstock: (a) 25% fill, (b) 50% fill, (c) 75% fill and (d) 100% fill. (e–h) Progressive filling of the heat sink substrate with fins shown in Fig. 5(b) for the 0.60 volume fraction bimodal μ–n AlN feedstock: (e) 25% fill, (f) 50% fill, (g) 75% fill and (h) 100% fill.

mold temperature using the heat-sink geometries shown in Fig. 5. The simulations were performed for mold filling and packing stages. The progressive filling behavior of the bimodal μ–n AlN feedstock (0.6 volume fraction) is shown in Fig. 6 for the two heat-sink geometries. The figure clearly shows that the narrow fin region of the mold cavity fills at the end of the molding stage, when the material is at its most viscous state (lowest bulk temperature).

Fig. 7 shows the variation of part weight as a function of volume fraction of bimodal μ–n AlN for the two heat-sink geometries shown in Fig. 5. The part weight increases with an increase in volume fraction of bimodal μ–n AlN powder from 0.52 to 0.60. This increase in part weight with an increase in powder volume fraction can be attributed to an increase in density values with a rise in volume fractions of bimodal μ–n AlN as observed in Table 4. Furthermore, for a bimodal μ–n AlN powder volume fraction change from 0.52 to 0.60, the part weight changes from 0.38 to 0.41 g for heat sink substrate without fins. In the case of the heat sink substrate with fins, the corresponding change is from 0.79 to 0.82 g. This change denotes a ±2% variation in part weight for a ±7% change in the volume fraction of bimodal μ–n AlN. The part weight doubled for heat sink substrate with fins in comparison to the heat sink substrates without fins.

As the filling phase nears completion, the packing phase commences during which the part cools till a 100% frozen volume is obtained. Fig. 8 shows the dependence on freeze time on the volume fraction of bimodal μ–n AlN powder in the feedstock, based on simulations. It can be observed from Fig. 8 that for a change of 0.52–0.60 volume fraction of bimodal μ–n AlN, the freeze time changes from 2.16 to 2 s for heat sink substrate without fins. In the case of the heat-sink substrate with fins, the change in freeze time is from 2.45 to 2.35 s. This denotes a ±2% variation in freeze time for a ±7% change in the volume fraction of bimodal μ–n AlN. The change in freeze-time as a function of volume fraction can be attributed to the change in thermal properties shown in Tables 5 and 6. The freeze time depends on material properties such as specific heat and thermal conductivity. With an increase in volume fraction of the powder, the specific heat of the feedstock decreases while the thermal conductivity increased. The interrelationship between the feedstock properties on the freeze time could explain the unsteady nature of the data in Fig. 8. In the future, further molding simulations and experiments need to be performed over a broad range of process conditions to better elucidate this behavior.

Fig. 9 show the variation in peak injection pressure as a function of the volume fraction of powder for the two heat-sink substrates, based on simulations. The peak injection pressure is located near the gate of the mold cavity. The peak injection pressure is relatively higher for the heat-sink substrate with fins compared to the heat-sink substrate without fins as a result of an increase in volumetric flow rate. It can be seen that for the heat-sink substrate with fins, the peak injection pressure increases from 23 to 48 MPa with an increase in powder volume fraction from 0.52 to 0.60. This behavior can be attributed to an increase in the viscosity of the powder–polymer mixture with volume fraction of bimodal μ–n AlN. An increase in injection pressure directly increases the clamp

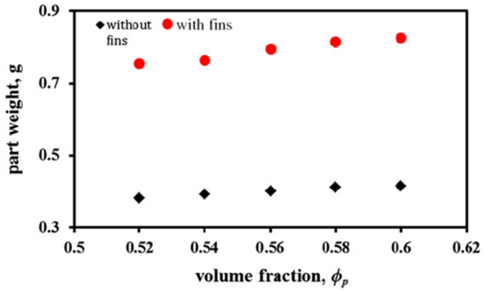

Fig. 7. Part weight for feedstocks with different volume fractions of bimodal μ–n AlN powder.

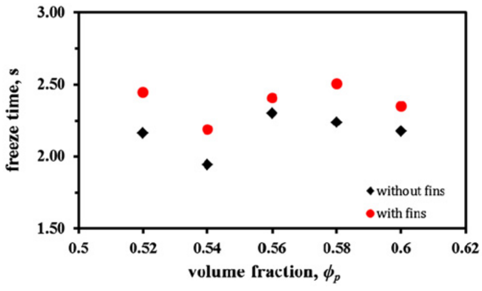

Fig. 8. Freeze time for feedstocks with different volume fractions of bimodal μ–n AlN powder.

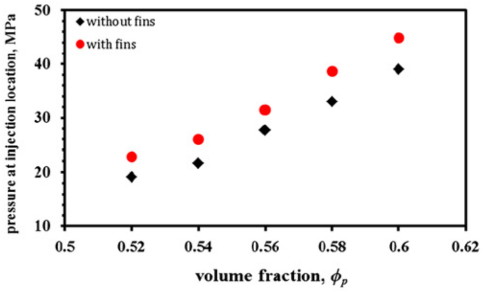

Fig. 9. Peak injection pressure for feedstocks with different volume fractions of bimodal μ–n AlN powder.

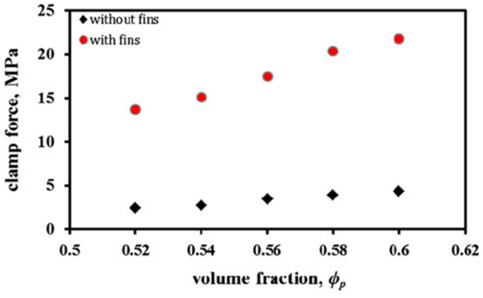

Fig. 10. Variation of clamp force for feedstocks with different volume fractions of bimodal μ–n AlN powder.

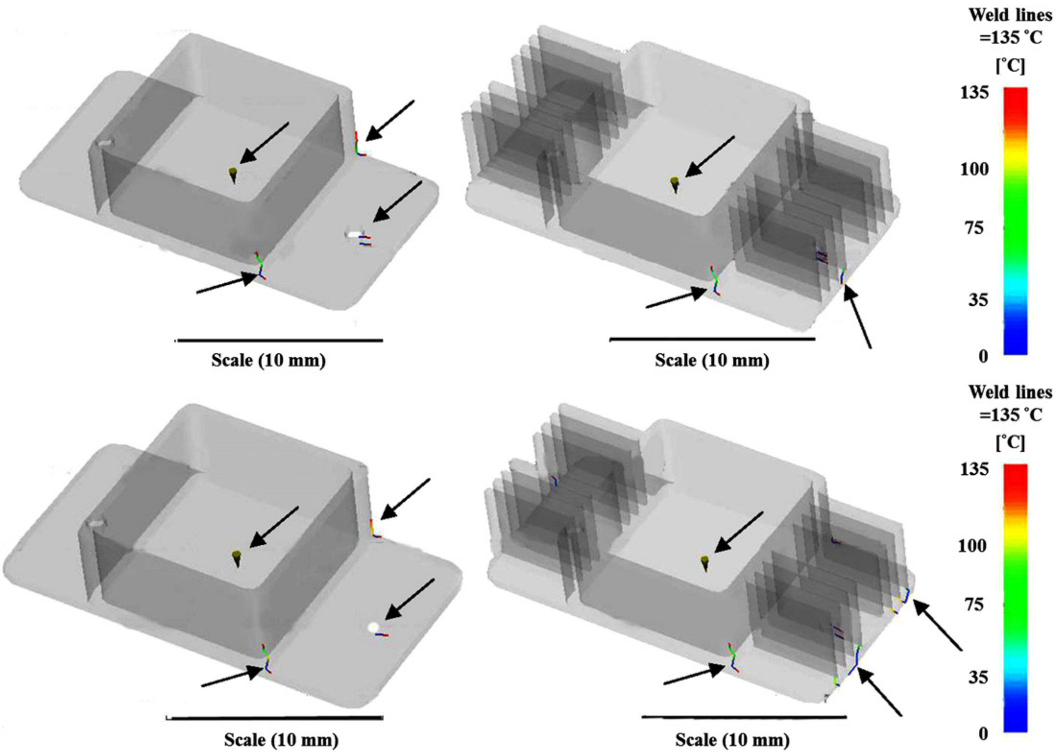

Fig. 11. Simulation results of weld lines at 0.52 volume fraction (top) and 0.6 volume fraction (bottom) bimodal μ–n AlN powder for heat sink geometry with and without fin. The arrows represent critical areas for formation of defects.

force (Fig. 10) and correspondingly reduces the number of mold cavities that can be simultaneously filled on a molding machine. An increase in injection pressure can also result in an undesirable alteration of the melt flow such as jetting. Furthermore, microstructural inhomogeneity can also be introduced in the part at higher injection pressures due to powder–polymer separation. Further experimental and simulations work is needed to correlate the influence of injection pressure on such molding defects.

3.3. Defect quality

Fig. 11 shows the weld-line distribution for the two heat-sink substrates at 0.52 and 0.60 volume fraction of bimodal μ–n AlN, based on simulations. No significant differences were observed for the weld-line distributions in the heat-sink substrate without fins as the powder volume fraction increased from 0.52 to 0.60. In contrast, a number of new weld lines appeared in the fin region of the second heat-sink substrate when the powder volume fraction increased from 0.52 to 0.60. The results suggest that the probability of defect evolution increases with increase in complexity of the part geometry and material composition.

4. Conclusions

The effects of nanoparticle addition and overall powder content on the rheological and thermal properties of a bimodal μ–n AlN feedstock were studied in the present paper using experimental measurements and mathematical models. The addition of nanoparticles showed a significant effect on the rheological properties of the feedstock, owing to an increase in the maximum packing fraction in the powder–polymer mixtures. The zero-shear viscosity, melt density, solid density, thermal conductivity, elastic and shear modulus increased with the increase in volume fraction of the powders. On the other hand, properties like specific volume, coefficient of thermal expansion and specific heat decreased with the increase in volume fraction of powder. Mold-filling simulation studies were performed using the experimentally measured and estimated feedstock properties. The simulations showed an increase in part weight and peak injection pressure with the increase in powder volume fraction. The studies also showed a decrease in freeze time with an increase in powder content. The combined protocols for feedstock property estimations and mold-filling simulations presented in the paper can be used to design new materials, select component geometrical attributes, and optimize process parameters while eliminating expensive and time-consuming trial-and-error practices prevalent in PIM.

Acknowledgment

S.V. Atre would like to acknowledge financial support from the National Science Foundation (Award no. CMMI 1200144).

References

[1] D.F. Heaney, Handbook of Metal Injection Molding, Woodhead Publishing Limited, Cambridge, UK, 2012.

[2] R.M. German, Powder Metallurgy Science, Metal Powder Industries Federation, 105 College Rd. E, Princeton, NJ 08540, USA, 1984.

[3] R.K. Enneti, S.J. Park, R.M. German, S.V. Atre, Review: thermal debinding process in particulate materials processing, Materials and Manufacturing Processes 27 (2012) 103–118.

[4] R.M. German, S.J. Park, Mathematical Relations in Particulate Materials Processing: Ceramics, Powder Metals, Cermets, Carbides, Hard Materials, and Minerals, John Wiley & Sons, 2008.

[5] V.P. Onbattuvelli, R.K. Enneti, S.V. Atre, The effects of nanoparticle addition on the sintering and properties of bimodal μ–n AlN, Ceramics International 38 (8) (2012) 6495–6499.

[6] V.P. Onbattuvelli, R.K. Enneti, S.V. Atre, The effects of nanoparticle addition on the densification and properties of SiC, Ceramics International 38 (7) (2012) 5393–5399.

[7] V.P. Onbattuvelli, The Effects of Nanoparticle Addition on the Processing, Structure and Properties of SiC and AlN, Thesis/Dissertation, 2010.

[8] V.P. Onbattuvelli, R.K. Enneti, S.J. Park, S.V. Atre, The effects of nanoparticle addition on SiC and AlN powder–polymer mixtures: packing and flow behavior, International Journal of Refractory Metals and Hard Materials 36 (2013) 77–84.

[9] K.H. Kate, V.P. Onbattuvelli, R.K. Enneti, S.W. Lee, S.J. Park, S.V. Atre, Measurements of powder–polymer mixture properties and their use in powder injection molding simulations for aluminum nitride, Journal of the Minerals, Metals & Materials Society 64 (9) (2012) 1048–1058.

[10] V.P. Onbattuvelli, S. Vallury, T. McCabe, S.J. Park, S. Atre, Properties of SiC and AlN feedstocks for the powder injection moulding of thermal management devices, Powder Injection Moulding International 4 (3) (2010) 64–70.

[11] X.Z. Shi, M. Huang, Z.F. Zhao, C.Y. Shen, Nonlinear fitting technology of 7-parameter Cross-WLF viscosity model, Advanced Materials Research 189–193 (2011) 2103–2106.

[12] L.E. Nielsen, Predicting the Properties of Mixtures: Mixture Rules in Science and Engineering, Marcel Dekker, 1978.

[13] H.H. Chiang, C.A. Hieber, K.K. Wang, A unified simulation of the filling and postfilling stages in injection molding, Part I: formulation, Polymer Engineering and Science 31 (2) (1991) 116–124.

[14] A. Boudenne, L. Ibos, M. Fois, E. Gehin, J.C. Majeste, Thermophysical properties of polypropylene/aluminum composites, Journal of Polymer Science Part B: Polymer Physics 42 (4) (2004) 722–732.

[15] D.T. Jamieson, G. Cartwright, Properties of Binary Liquid Mixtures: Heat Capacity, National Engineering Laboratory, 1978.

[16] B. Weidenfeller, M. Höfer, F.R. Schilling, Thermal conductivity, thermal diffusivity, and specific heat capacity of particle filled polypropylene, Composites Part A 35 (4) (2004) 423–429.

[17] G. Subodh, M.V. Manjusha, J. Philip, M.T. Sebastian, Thermal properties of polytetrafluoroethylene/$Sr_2Ce_2Ti_5O_{16}$ polymer/ceramic composites, Journal of Applied Polymer Science 108 (3) (2008) 1716–1721.

[18] C.P. Wong, R.S. Bollampally, Thermal conductivity, elastic modulus, and coefficient of thermal expansion of polymer composites filled with ceramic particles for electronic packaging, Journal of Applied Polymer Science 74 (14) (1999) 3396–3403.

[19] H. Ishida, S. Rimdusit, Heat capacity measurement of boron nitride-filled polybenzoxazine: the composite structure-insensitive property, Journal of Thermal Analysis and Calorimetry 58 (3) (1999) 497–507.

[20] C.P. Wong, R.S. Bollampally, Thermal conductivity, elastic modulus, and coefficient of thermal expansion of polymer composites filled with ceramic particles for electronic packaging, Journal of Applied Polymer Science 74 (14) (1999) 3396–3403.

[21] G.-W. Lee, M. Park, J. Kim, J.I. Lee, H.G. Yoon, Enhanced thermal conductivity of polymer composites filled with hybrid filler, Composites Part A 37 (5) (2006) 727–734.

[22] D.C. Moreira, L.A. Sphaier, J.M.L. Reis, L.C.S. Nunes, Experimental investigation of heat conduction in polyester–Al_2O_3 and polyester–CuO nanocomposites, Experimental Thermal and Fluid Science 35 (7) (2011) 1458–1462.

[23] Y. Xu, D.D. Chung, C. Mroz, Thermally conducting aluminum nitride polymer–matrix composites, Composites Part A 32 (12) (2001) 1749–1757.

[24] T.K. Dey, M. Tripathi, Thermal properties of silicon powder filled high-density polyethylene composites, Thermochimica Acta 502 (1–2) (2010) 35–42.

[25] K. Sanada, Y. Tada, Y. Shindo, Thermal conductivity of polymer composites with close-packed structure of nano- and micro-fillers, Composites Part A 40 (6–7) (2009) 724–730.

[26] P. Badrinarayanan, M.R. Kessler, Zirconium tungstate/cyanate ester nanocomposites with tailored thermal expansivity, Composites Science and Technology 71 (11) (2011) 1385–1391.

[27] S. Tognana, W. Salgueiro, A. Somoza, J.A. Pomarico, H.F. Ranea-Sandoval, Influence of the filler content on the thermal expansion behavior of an epoxy matrix particulate composite, Materials Science and Engineering: B 157 (1–3) (2009) 26–31.

[28] S. Elomari, R. Boukhili, D.J. Lloyd, Thermal expansion studies of prestrained Al_2O_3/Al metal matrix composite, Acta Materialia 44 (5) (1996) 1873–1882.

[29] K.H. Kate, R.K. Enneti, S.J. Park, R.M. German, and V. Atre, Predicting powder–polymer mixture properties for PIM design, International Materials Reviews, submitted for publication.